# A Model of Radar Backscatter of Rain-Generated Stalks on the Ocean Surface

Xinan Liu, *Member, IEEE*, Quanan Zheng, Ren Liu, *Student Member, IEEE*,
Mark A. Sletten, *Senior Member, IEEE*, and James H. Duncan

*Abstract*— In this paper, a model of radar backscattering from rain-generated stalks on the ocean surface in a rain field is proposed. In the model, stalks in the rain field form an array and are considered as finite water cylinders standing out of an infinite water surface. The radar backscattering coefficient from these stalks is derived. Both incoherent and coherent backscattering mechanisms from the stalks are considered. The model shows that the radar backscattering intensity is a function of the average distance between stalks on the water surface, the radar wave frequency, and the incident angle of radar waves. For light/moderate rain (at low rain rates), the radar backscattering intensity increases with increasing rain rate. For heavy rain (at high rain rates), the radar backscattering intensity decreases with increasing rain rate. The maximum radar backscattering intensity occurs at a rain rate that depends on the radar wave frequency and the incident angle of radar waves. The present model is used to explain the radar signatures of a rainfall event simultaneously observed by C-band ENVISAT (European satellite) Advanced Synthetic Aperture Radar (ASAR) and ground-based weather radar in the Northwest Pacific. The relationship between the radar return intensity extracted from the C-band ASAR image and the rain rate obtained from ground-based weather radar is in agreement with the model's calculation. Also, the air–sea interface in rain fields and its effects on the attenuation of radar backscattering are experimentally studied in the laboratory.

*Index Terms*— Radar scattering, rainfall effects, surface waves, synthetic aperture radar (SAR).

## I. INTRODUCTION

OCEANIC rainfall has been frequently observed in space-borne synthetic aperture radar (SAR) images since the first SAR image became available in 1978 [1]–[3]. Using SAR images, many interesting details of rainfall events over the ocean have been reported and qualitatively analyzed [4]–[6]. For instance, on a typical SAR image for convective rain, rain cells on the ocean surface usually show up as circular or oval bright patterns with sharp edges [1], [4]. In most cases,

there is a dark patch at the center of the SAR signature of a rain cell. The bright patterns are interpreted in [7] and [8] as the results of the cool downdraft accompanying the rain reaching the ocean surface and diverging to become horizontal winds. These winds generate surface waves that have Bragg wavelengths and are detectable by the radar. It is argued that the formation of dark patches at the centers of rain cells may be due to the damping of surface waves by rain-induced turbulence or the raindrops in the atmosphere for X- and C-band radar signatures [9].

The radar signatures of a rainfall event over the ocean are mainly generated from the scattering and attenuation of the microwaves by raindrops in the atmosphere and from the scattering by the sea surface features that are associated with raindrop impacts and wind. The effects of raindrops on the scattering and attenuation of the microwaves in the atmosphere have been extensively studied by radar meteorologists [10]. The scattering is described by a volume backscattering coefficient that is a function of the radar wavelength, the refractive index of water, and the reflectivity of raindrops, while the attenuation is depicted by a volume attenuation coefficient that depends on a power law function of the rain rate [11]. In a rain/wind backscatter model recently developed in [12], both the scattering and attenuation effects of raindrops in the air were considered. Thereafter, a more sophisticated physics-based radiative transfer model in [13] also considers the ring waves generated by rain as discussed below.

The effects of rainfall on radar scattering from a water surface were first investigated in [14]. Further investigations on this subject with different microwave frequencies were performed in [15]–[17] and others. Radar backscatters from the ocean surface in a rain field are mainly produced by surface waves and the splash products of raindrop impacts. The surface waves are generated by wind and altered by rain in a number of ways. When raindrops impinge on the ocean surface, they generate ring (gravity-capillary) waves on the water surface and turbulence beneath the water surface. Laboratory experiments performed by a number of investigators [17]–[21] showed that rain-induced turbulence damps mechanically generated gravity waves and wind waves with wavelengths larger than several centimeters. At the same time, capillary-gravity waves are enhanced by rain-generated ring waves. In the absence of wind, the frequency spectra of gravity-capillary ring waves generated by rain are of a log-Gaussian form [22]–[24]. The spectral peak frequency of the ring waves decreases as the raindrop diameter increases, but is nearly

independent of the rain rate. Based on momentum exchange, a theoretical model for determining the dynamic effects of rain intensity on water waves has been developed in [25]. It was found that for vertical or near-vertical rainfall, the rain causes nonnegligible wave amplitude decay. In high winds, the rain enhances high-frequency waves because the horizontal velocity component of the rain is large and the corresponding stress on the free surface is nearly in phase with the free surface slope.

A number of radar backscattering models considering the effects of rain on the ocean surface waves have been developed to understand and interpret various phenomena, such as wind fields, hurricanes, and tropical cyclones observed by SAR [13], [26], [27]. A numerical model of surface wind waves modified by rainfall and the backscattering of microwaves from these modified surface waves has been developed in [27]. The effects of both rain-induced damping and the enhancement of gravity-capillary waves due to the presence of ring waves were considered in the model. Several commonly used microwave frequencies were simulated to investigate the effects of rain on the backscatter from the ocean. A similar model for hurricane rain given in [26] considered the effects of long waves that alter the local incident angles and polarizations of radar waves, and the volume scattering and attenuation of raindrops in the air.

The effects of the splash products of raindrop impacts on the radar backscattering are rarely studied. The splash products include crowns, stalks, cavities, and secondary drops. In [16], the surface features generated by single drop impacts were measured with a high-speed digital camera that was synchronized with radar data acquisition. The radar backscattering powers from crowns, craters, stalks, and ring waves were compared and it is concluded that while ring-waves are the dominant scattering contribution, the scatterings from crowns, craters, and stalks are not negligible. A scattering model from the splash products of a single raindrop impact developed in [28] shows that the stalk has significant effects on the major scattering features. In [29], the radar signatures of a rainfall event simultaneously observed by C-band ENVISAT (European satellite) Advanced SAR (ASAR) and ground-based weather radar in the Northwest Pacific were analyzed. It was found that the spaceborne radar backscattering intensity strongly correlates with the average distance of the stalks on the water surface in the rain field in a nonlinear manner.

Based upon the analysis of published data and the experimental results obtained in the laboratory, [29] showed the following.

1) Among the surface features generated by raindrop impacts (including ring waves, stalks, crowns, and secondary drops), stalks are dominant in terms of their height, lifetime, water mass, and energy.
2) Stalks are randomly distributed on the water surface in both time and position.
3) The average distance between two successive stalks decreases with increasing rain rate.
4) The measured stalk heights are well approximated by a Rayleigh distribution.
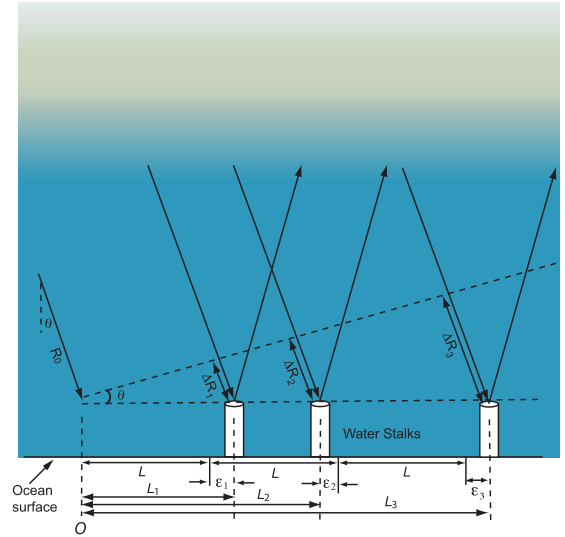


Fig. 1. Schematic showing the radar backscattering from stalks generated by rainfall on the ocean surface. The variation of the background color depicts the variation of water content in the air-water interface of rain field. The gray area close to the ocean surface represents a high-water-content layer of dense clouds of seawater droplets generated by rain (see Fig. 5).

In typical radar applications, the measured average stalk height $(\bar{h})$ exceeds the Rayleigh criterion, i.e., $\bar{h} > (\lambda/8\cos(\theta))$ where $\lambda$ is the radar wavelength and $\theta$ the incident angle of radar waves relative to the vertical. In this paper, we attempt to establish a scattering model that considers the rain-generated stalks on the ocean surface as alternative radar scatterers.

The remainder of this paper is organized as follows. Section II describes our physical model for radar scattering from water stalks that are generated by impinging raindrops on rain cells. In Section III, the model is discussed and is applied to interpret one rainfall event in the Northwest Pacific simultaneously observed by a ground-based weather radar located in southern Taiwan and the ASAR from the European satellite ENVISAT. The air–sea interface in rain fields and its effects on the attenuation of the radar backscattering from the stalks are explored. The conclusions are presented in Section IV.

## II. MODEL OF RADAR BACKSCATTERING FROM THE OCEAN SURFACE IN RAIN FIELD

In this paper, a model considering multiple raindrop splashes that intersect a single incident plane is proposed, as shown in Fig. 1. Cylinders, which are small compared to the radar wavelength, are used to represent the stalks generated by raindrops because of their similar radar scattering features in the microwave band [11]. These stalks are randomly distributed on the water surface and the average distance between two adjacent stalks is $L$. Thus, the distance of the $n$th cylinder away from the reference point $O$ along the line may be given as

$$L_n = nL + \epsilon_n \qquad (1)$$

where $\epsilon_n$ is a random variable describing the deviation of the distance of the $n$th cylinder from $nL$. It is obvious that the mean value of $\epsilon_n$ is zero. The single-trip difference of radar

waves between the $n$th ray path and the reference point is given as follows:

$$\Delta R_n = L_n \sin\theta = (nL + \epsilon_n)\sin\theta \tag{2}$$

where $\theta$ is the incident angle of radar waves relative to the vertical.

The received voltage from the oceanic rain field is the sum of the voltages from the individual cylinders [11], that is

$$V_r = \sum_{n=1}^{N} V_n e^{-i2k(R_0 + \Delta R_n)} \tag{3}$$

where $N$ is the total number of stalks in the resolution cell, $R_0$ is the radial distance to the radar antenna, $k(= 2\pi/\lambda)$ is the radar wavenumber, $\lambda$ is the radar wavelength, and $V_n$ is the received voltage from the $n$th stalk. Assuming that the radar waves along the two-way path of length $R_0 + \Delta R_n$ are exponentially attenuated [9], the received voltage $V_n$ can be expressed as

$$
\begin{aligned}
V_n &= V_0 s \exp\left[-2\int_0^{(R_0 + \Delta R_n)} \kappa(r)\, dr\right] \\
&\approx V_0 s \exp\left[-2\int_0^{R_0} \kappa(r)\, dr - 2\int_{R_0}^{(R_0 + nL\sin\theta)} \kappa(r)\, dr\right] \\
&= V_0 s e^{-2\alpha_1 R_0} \exp\left[-2\int_{R_0}^{(R_0 + nL\sin\theta)} \kappa(r)\, dr\right]
\end{aligned}
\tag{4}
$$

where $V_0$ is the incident voltage, $s$ is a factor that is related to the stalk backscatter cross section [28], $\alpha_1 = (1/R_0)\int_0^{R_0} \kappa(r)\, dr$, and $\kappa(r)$ is the attenuation coefficient that is assumed to vary along the path. The radar waves are attenuated by raindrops high above in the air. The attenuation rate of radar waves close to the ocean surface dramatically increases due to a high-water-content layer of dense clouds of seawater droplets generated by the rain (see Fig. 5).

Assuming that $\kappa(r) = \alpha_2$ is a constant within this high-water-content layer yields

$$
\begin{aligned}
\exp\left[-2\int_{R_0}^{(R_0 + nL\sin\theta)} \kappa(r)\, dr\right] &= e^{-2\alpha_2 nL\sin\theta} \\
&= (e^{-2\alpha_2 L\sin\theta})^n
\end{aligned}
\tag{5}
$$

and (4) becomes

$$V_n = V_0 S \beta^n \tag{6}$$

where $S = se^{-2\alpha_1 R_0}$ and $\beta = e^{-2\alpha_2 L\sin\theta}$ $(0 < \beta < 1)$ is the damping coefficient. It is worth stressing that the parameter $\alpha_1$ mainly describes the attenuation of radar waves caused by raindrops in the atmosphere, while $\alpha_2$ and $\beta$ depict the attenuation of radar waves due to the dense clouds of seawater droplets generated by the rain.

One issue is that the present model is 1-D while the rain-generated stalks on the ocean surface are distributed in 2-D space. To resolve this issue, we applied the fact that the radar backscatter at any instant of time is the coherent sum of the individual echoes produced by multiple stalks, all located at the same radial distance from the radar antenna. In other words, these stalks are within the wavefront that intersects the water surface and is locally perpendicular to the propagation direction of the radar waves. Thus, the height of each cylinder

in the model is approximated by the average height of the stalks mentioned above. As for a homogeneous rain field, the heights of these cylinders vary slightly along the propagation direction of the radar waves. The prediction of the cross-sectional factor of these cylinders, i.e., the parameter $s$, can be found in [28].

Substituting (2) and (6) into (3) yields

$$
\begin{aligned}
V_r &= V_0 S e^{-i2kR_0} \sum_{n=1}^{N} \beta^n e^{-i2k(nL+\epsilon_n)\sin\theta} \\
&= V_0 S e^{-i2kR_0} \sum_{n=1}^{N} \beta^n e^{-in\phi} e^{-iz_n}
\end{aligned}
\tag{7}
$$

where $\phi = 2kL\sin\theta = 4\pi\frac{L}{\lambda}\sin\theta$ and $z_n = 2k\epsilon_n\sin\theta = \phi\frac{\epsilon_n}{L}$. Using the Taylor series expansion of $e^{-iz_n}$ at $z_n = 0$, (7) becomes

$$
\begin{aligned}
V_r &= V_0 S e^{-i2kR_0} \sum_{n=1}^{N} \beta^n e^{-in\phi}\left(1 - iz_n - \frac{z_n^2}{2} + i\frac{z_n^3}{3!}\right. \\
&\qquad\qquad \left. + \frac{z_n^4}{4!} - i\frac{z_n^5}{5!} - \frac{z_n^6}{6!} + \cdots\right) \\
&= V_0 S e^{-i2kR_0} \sum_{n=1}^{N} \beta^n e^{-in\phi} - V_0 S e^{-i2kR_0} \sum_{n=1}^{N} \beta^n e^{-in\phi} \\
&\quad \times \left(iz_n + \frac{z_n^2}{2} - i\frac{z_n^3}{3!} - \frac{z_n^4}{4!} + i\frac{z_n^5}{5!} + \frac{z_n^6}{6!} - \cdots\right).
\end{aligned}
\tag{8}
$$

It should be mentioned that since $z_n$ is a real number, $e^{-iz_n}$ is periodic with a period of $2\pi$ and an amplitude of 1. In our model, the range of $\epsilon_n$ is converted into $[-(\pi L/\phi), (\pi L/\phi)]$ using the period, i.e., $\epsilon_n \bmod (\pi L/\phi)$, so that the Taylor series for $e^{-iz_n}$ are given in the principal argument of $e^{-iz_n}$, i.e., $-\pi \le z_n \le \pi$. Seven terms of the Taylor series provide sufficient accuracy for the approximation.

The first term on the right-hand side of (8) depicts the coherent backscattering voltage from the stalks and is denoted by

$$V_{rC} = V_0 S e^{-i2kR_0} \sum_{n=1}^{N} \beta^n e^{-in\phi}. \tag{9}$$

The coherent scattering of microwaves by particles in the atmosphere has been studied in [30] and evidence of the radar coherent backscattering from clouds and smoke is provided, based on the field measurement data given in [31] and [32], respectively. Some direct observations of radar coherent backscattering signals in both natural rain and snow fields were given in [33]–[36].

Using the following mathematical identity for a large $N$

$$\lim_{N\to\infty}\left(\sum_{n=1}^{N} \beta^n e^{-in\phi}\right) = \frac{(\beta\cos\phi - \beta^2) - i\beta\sin\phi}{1 - 2\beta\cos\phi + \beta^2} \tag{10}$$

(9) becomes

$$V_{rC} = V_0 S \frac{\beta\cos\phi - \beta^2 - i\beta\sin\phi}{1 - 2\beta\cos\phi + \beta^2} e^{-i2kR_0}. \tag{11}$$

The second term on the right-hand side of (8) describes the incoherent backscattering voltage from the stalks due to their randomness in space and can be rewritten as follows:

$$V_{rI} = V_0 S\phi e^{-i2kR_0} \sum_{n=1}^{N} \frac{\epsilon_n}{L}\beta^n (1 - \frac{z_n^2}{3!} + \frac{z_n^4}{5!}) e^{-i(n\phi+\pi/2)}$$
$$- V_0 S\phi^2 e^{-i2kR_0} \sum_{n=1}^{N} \left(\frac{\epsilon_n}{L}\right)^2 \beta^n \left(\frac{1}{2} - \frac{z_n^2}{4!} + \frac{z_n^4}{6!}\right) e^{-in\phi}.$$
$$(12)$$

Furthermore, the radar backscattering coefficient is defined as

$$\sigma = \frac{|V_r|^2}{|V_0|^2} = \frac{|V_{rC}|^2}{|V_0|^2} + \frac{|V_{rI}|^2}{|V_0|^2} = \sigma_0 + \sigma_I. \qquad (13)$$

where

$$\sigma_0 = \frac{S^2\beta^2}{1 - 2\beta \cos(4\pi \frac{L}{\lambda}\sin\theta) + \beta^2} \qquad (14)$$

and

$$\sigma_I = S^2\phi^2 \sum_{n=1}^{N} |\frac{\epsilon_n}{L}|^2 \beta^{2n} \left(1 - \frac{\phi^2}{3}|\frac{\epsilon_n}{L}|^2 + \frac{2\phi^4}{45}|\frac{\epsilon_n}{L}|^4 \right.$$
$$\left. - \frac{\phi^6}{360}|\frac{\epsilon_n}{L}|^6 + \frac{\phi^8}{120^2}|\frac{\epsilon_n}{L}|^8\right)$$
$$+ S^2 \frac{\phi^4}{4} \sum_{n=1}^{N} |\frac{\epsilon_n}{L}|^4 \beta^{2n} \left(1 - \frac{\phi^2}{6}|\frac{\epsilon_n}{L}|^2 + \frac{\phi^4}{80}|\frac{\epsilon_n}{L}|^4 \right.$$
$$\left. - \frac{\phi^6}{2160}|\frac{\epsilon_n}{L}|^6 + \frac{\phi^8}{360^2}|\frac{\epsilon_n}{L}|^8\right).$$
$$(15)$$

Equation (14) shows that the radar coherent backscattering coefficient ($\sigma_0$) from the stalks is a function of the damping coefficient ($\beta$), the incident angle of radar waves ($\theta$), the ratio of the distance between two adjacent stalks and the wavelength of radar waves ($L/\lambda$), and the parameter $S$. For given $\beta$ and $S$, the radar backscattering coefficient varies with the ratio $L/\lambda$ and has a period of $1/(2\sin\theta)$. Fig. 2 shows $\sigma_0$ versus $L/\lambda$ with $\beta = 0.5$ and $S = 1$ for three angles of incidence of the radar waves. As can be seen from Fig. 2, the variation of the radar backscattering coefficient with $L/\lambda$ is drastically affected by the incidence angle of the radar waves. The value of $L/\lambda$ corresponding to the peak radar backscattering coefficient changes with the incidence angle. For an incidence angle of $\theta = 30°$, the maximum radar backscattering coefficient occurs at $L/\lambda = 1$. This indicates that a strong radar backscattering signal may be received when the distance between two adjacent stalks is equal to the wavelength of radar waves for that incidence angle. The backscattering peaks shown in Fig. 2 likely result from a Bragg resonance process with uniformly spaced stalks.

Equation (15) shows the radar incoherent backscattering coefficient from the stalks due to the randomness ($\epsilon_n$) of the stalks in space. It should be realized that it is difficult to calculate $\sigma_I$ from (15) because the distribution of $\epsilon_n$ is unknown and $\epsilon_n$ is included in the coefficients of the power series of $\beta$. Field measurements are needed to determine
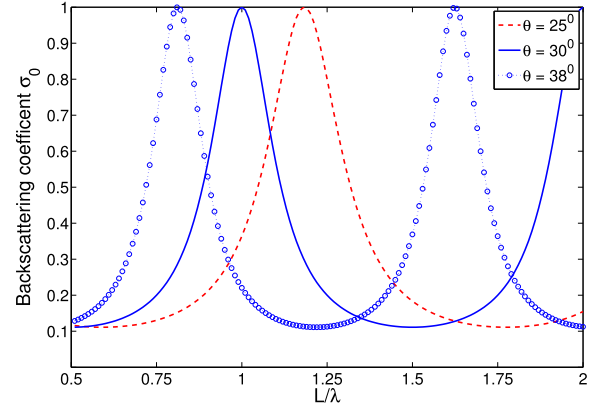


Fig. 2. Radar backscattering coefficient $\sigma_0$ varies with $L/\lambda$ at three incident angles of radar waves.

the distribution of random distances ($\epsilon$) between the stalks in space. However, the upper bound of $\sigma_I$ may be estimated using $\beta = 1$ (the upper limit of $\beta$) as follows:

$$\sigma_{Iu} = NS^2\phi^2 \left(\mu_2 - \frac{\phi^2}{12}\mu_4 + \frac{\phi^4}{360}\mu_6 + \frac{\phi^6}{2880}\mu_8 \right.$$
$$\left. - \frac{\phi^8}{21600}\mu_{10} + \frac{\phi^{10}}{720^2}\mu_{12}\right) \quad (16)$$

where $\mu_m = (1/N)\sum_{n=1}^{N} |(\epsilon_n/L)|^m$, $(m = 2, 4, \ldots, 12)$ is the $m$th central moment of the random variable $\epsilon_n/L$. As can be seen from (16), the upper bound of the radar incoherent backscattering coefficient ($\sigma_{Iu}$) is primarily proportional to the variance $\mu_2$. For a highly random distribution of $\epsilon_n/L$ (large value of $\mu_2$), $\sigma_{Iu}$ is greater than $\sigma_0$, indicating that the incoherent backscattering from the stalks is dominant, which will be discussed in a separate paper.

## III. DISCUSSION

### A. Dependence of Radar Signatures on Radar Wave Frequency

The SAR images of a large number of oceanic rainfall events [5], [9] show that the radar backscattering intensity varies with the radar frequency. This characteristic of radar wave frequency dependence can be qualitatively explained by the model developed in this paper. Based on published data, the spatial characteristics of raindrops in rain fields were analyzed in [29]. The average distance between adjacent raindrops is a function of the rain rate as follows:

$$L = \sqrt[3]{\frac{5.17\pi \times 10^5}{1 + 7.79R^{-0.21}}} \; R^{-0.12} \qquad (17)$$

where $R$ is the rain rate in mm/h. It is assumed that the average distance between adjacent rain-generated stalks on the ocean surface is equal to the average distance between raindrops in the air. Substituting (17) into (14) yields a radar backscattering coefficient that varies with the rain rate. Fig. 3 shows the radar backscattering coefficient $\sigma_0$ versus the rain rate for three radar wave frequencies (L-, C-, and X-band) at an incident angle $\theta = 38°$ with $\beta = 0.5$ and $S = 1$. As can be seen from Fig. 3, for all the three radar wave frequencies, the radar
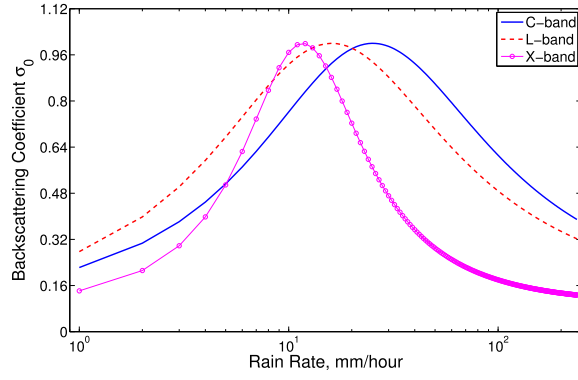
Fig. 3. Radar backscattering coefficient $\sigma_0$ varies with the rain rate $R$ for three radar wave frequencies (L-, C-, and X-band). The wavelengths of L-, C-, and X-band radar waves are 235, 57, and 30 mm, respectively. The incident angle $\theta = 38°$, $\beta = 0.5$, and $S = 1$.

backscattering coefficients increase with an increasing rain rate for light/moderate rain (at low rain rates), but decrease with an increasing rain rate for heavy rain (at high rain rates). The maximum radar backscattering coefficients occur at rain rates that vary with the radar wave frequency. The rain rates corresponding to the maximum radar backscattering coefficients of $L$-, $C$-, and X-band radar waves are 16, 24, and 12 mm/h, respectively. For rain rates greater than 24 mm/h, the radar backscatter of C-band waves is the strongest while the radar backscatter of X-band waves is the weakest. To some extent, this is consistent with that observed from SAR images (see [9, Fig. 9(a)]). However, direct comparison between the present model and the data shown in [9] is not available due to the lack of rain rates in that paper.

### B. Interpretation of SAR Images of the Rainfall Over the Ocean

The radar backscattering model proposed in this paper is used to interpret the radar signatures of a rainfall event in the Northwest Pacific simultaneously observed by the C-band ASAR from the European Satellite ENVISAT and ground-based weather radar. Both the SAR images and the ground-based weather radar image have been described in [29]. The SAR images were obtained with C-band radar waves with wavelength $\lambda = 5.7$ cm and the incident angle of the radar waves was $\theta = 38°$. Fig. 4 shows the radar backscattering coefficients (data points with error bars) measured from an SAR image versus the corresponding rain rate obtained from ground-based weather radar. The detailed procedure of the data analysis can be found in [29]. As can be seen from Fig. 4, while the radar backscattering intensity from satellite ($\sigma_M$) does not increase monotonically with the rain rate ($R$), its response can be divided into three regions. For light rain with the rain rate ranging from 0.1 to 1.0 mm/h, the radar backscattering intensity has little change with the rain rate. For moderate rain with the rain rate ranging from 1.0 to 24 mm/h, the radar backscattering intensity increases gently with the rain rate. For heavy rain with the rain rate ranging from 24 to 167 mm/h, the radar backscattering intensity decreases quickly with the rain rate. The maximum radar backscattering intensity occurs approximately at a rain rate of 24 mm/h.
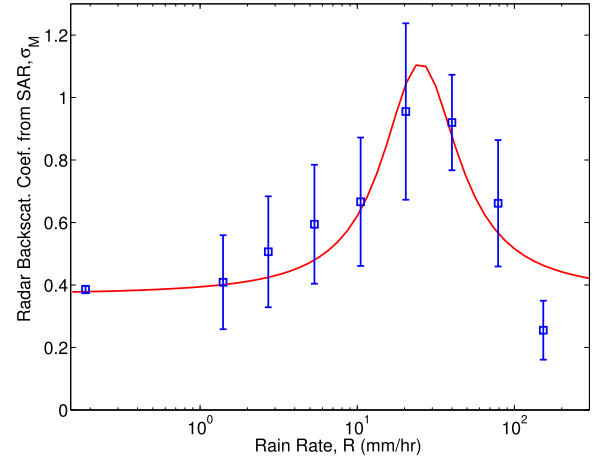


Fig. 4. Observed dependence of C-band ASAR radar backscattering coefficient on the radar reflectivity factor for the rain system on the ocean surface. Data points from [29] represent statistical means and standard deviations of radar backscattering coefficient from the satellite data. The solid line is obtained from (14), (17), and (18) with $\beta = 0.75$, $S = 0.083$, $\lambda = 57$ mm, $\theta = 38°$, $\sigma_{sw} = 0.38$, $\alpha_{atm} = 1$, and $\sigma_{atm} = 0$.

Using a similar approach as that shown in [12], the space-borne radar backscattering coefficient $\sigma_M$ measured from a rain field over the ocean may be represented as follows:

$$\sigma_M = (\sigma_{sw} + \sigma_{spl})\alpha_{atm} + \sigma_{atm} = \sigma_{sw}\alpha_{atm} + \sigma_0 + \sigma_{atm} \quad (18)$$

where $\sigma_{sw}$ is the backscatter of the surface waves in the rain field, $\sigma_{spl}$ is the backscatter of the splash products of raindrop impacts, which include stalks only in this paper, $\alpha_{atm}$ is the two-way rain-induced atmospheric attenuation, and $\sigma_{atm}$ is the rain-induced atmospheric backscatter. The surface waves consist of the wind waves that are modified by rain and the ring waves generated by the impacts of raindrops. The radar backscatter from the stalks consists of both coherent and incoherent components as shown in the previous section. Since $\phi = 2kL\sin\theta$ and $L$ decreases as the rain rate increases [see (17)], (16) shows that $\sigma_{Iu}$ decreases with increasing rain rate. However, the data points in Fig. 4 show that for light rain, the radar backscattering from the rain field increases as the rain rate increases. This indicates that $\mu_2$ has to be small, otherwise radar backscattering would be high at low rain rates due to the effects of the randomness of the stalks in space. Thus, only the radar coherent backscattering coefficient from the stalks is used herein, i.e., $\sigma_{spl}\alpha_{atm} = \sigma_0$.

Since the effect of rain on the radar backscattering is of minor importance for light rain, i.e., $\sigma_{atm} \approx 0$, $\alpha_{atm} \approx 1$ and $\sigma_{spl} \approx 0$, using (18) and the left data point in Fig. 4 yields $\sigma_{sw} = \sigma_M = 0.38$. As for the SAR images shown in [29] and used in this paper, the weather charts (see [29, Sec. 4]) show that at the time the SAR images were taken, the wind speed for most of the region of the rain system was approximately equal to 6 m/s. The fact that the waves between 5 and 10 cm length might be damped or enhanced by the rain [4], [17] makes a theoretical estimation of $\sigma_{sw}$ varying with the rain rate difficult. For instance, the numerical model in [27] showed that the radar backscattering coefficient increases slightly with increasing rain rate at an incident angle

of about 38°, while the model in [26] showed that the radar backscattering coefficient slightly decreases in the presence of rain with low wind speeds. Therefore, it is assumed herein that $\sigma_{sw}$ is a constant, disregarding the rain rate.

The solid line in Fig. 4 is computed from the present model with (14), (17), and (18). Since no measurement of $\beta$ can be found in the literature at this moment, it is assumed that $\beta$ is a constant. In addition, it is difficult to calculate $S$ because both the height of the hydrometers above the sea surface and the attenuation coefficient $\kappa(r)$ are unknown. Thus, the values of $\beta = 0.75$ and $S = 0.083$ in (14) are estimated by fitting (18) to the data points in Fig. 4 with $\sigma_{sw} = 0.38$, $\alpha_{\text{atm}} = 1$, and $\sigma_{\text{atm}} = 0$. As can be seen from Fig. 4, the relationship between the radar return intensity extracted from the C-band ASAR image and the rain rate obtained from ground-based weather radar agrees well with the model's calculation for rain rates less than 80 mm/h. For heavy rain ($R = 167$ mm/h), the calculation is higher than the satellite data, suggesting that the radar backscattering intensity is additionally attenuated by the raindrops in the air, i.e., $\alpha_{\text{atm}} < 1$ and/or the wind waves are damped by the rain-generated turbulence [29]. Using $\beta = e^{-2\alpha_2 L \sin\theta}$ yields $\alpha_2 \approx 0.041$ cm$^{-1}$ = $4.1 \times 10^3$ km$^{-1}$. However, the attenuation coefficient ($\alpha_1$) of C-band waves in the atmosphere with a rain rate of $R = 100$ mm/h is about 0.15 km$^{-1}$ [37], indicating that the attenuation of radar waves in the rain-generated layer with clouds of seawater droplets is much higher than that caused only by the raindrops high above in the air. A laboratory experiment described in the following section provides evidence of the high attenuation of radar waves in the air–sea interface of a rain field.

## C. Attenuation of Radar Waves in the Air–Sea Interface of a Rain Field

As discussed in Section II, the attenuation factor $\alpha_2$ occurs in the rain-generated layer close to the ocean surface, where the water content is high due to the dense clouds of seawater droplets and vapor formed by secondary drops, water stalks, crowns, waves, bubbles, and foam. A sample image given in Fig. 5 shows a low portion of the layer near the water surface. The image was taken in the laboratory with fresh clean water. The experimental setup is briefly described in the Appendix and the details can be found in [29]. In the image, round (oval) objects are the secondary drops while the raindrops appear as short vertical bars, as the velocity of the raindrops is much higher than that of the secondary drops. A long exposure time was used in order to obtain sharp images of the secondary drops that move at relatively slow speed. The horizontal line indicates the intersection of the focal plane of the camera and the water surface. As can be seen from the image, the number of secondary droplets with diameters similar to that of the raindrops is nearly 20 times higher than that of the raindrops in the same area. These large secondary drops can reach as high as 10 to 15 cm, indicating that the liquid water content in the low portion of the air layer is much higher than that far above where only raindrops are found. The layer with a dense population of secondary drops with diameters much less than that of the raindrops extends a height estimated by visual observation of about 0.5 m.
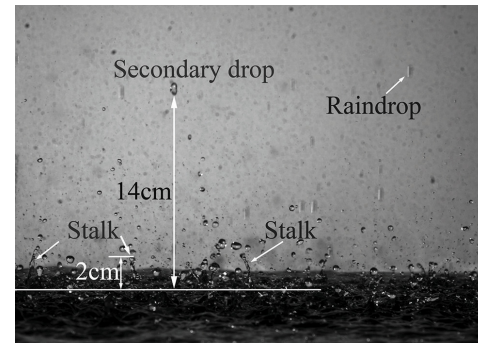


Fig. 5. Image showing secondary drops and raindrops in the air layer above the water surface. The round (oval) objects are secondary drops, while raindrops appear as short vertical bars as the velocity of the raindrops is much higher than that of the secondary drops and a long exposure time was used to obtain shape images of the secondary drops that move at relatively slow speed. The horizontal line indicates the intersection of the focal plane of the camera and the water surface. The heights of the stalks are about 2 cm.
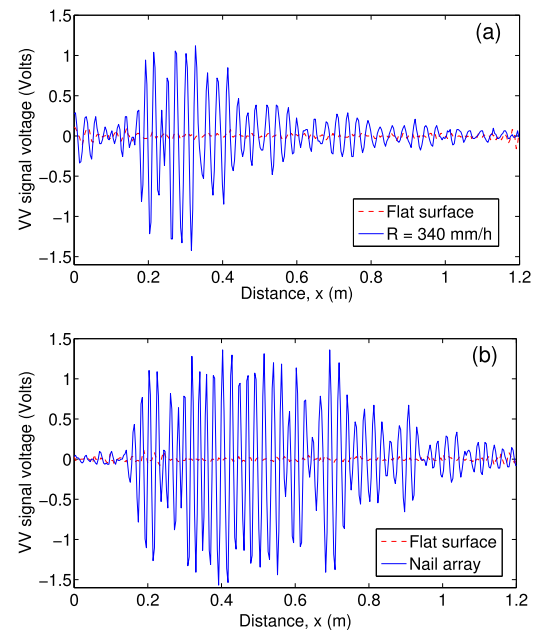


Fig. 6. Radar VV signals versus the distance from the antennas [$x = 0$ is the water tank edge close to the antennas (see Fig. 7)]. (a) Measured from the rain field. (b) Measured from the same raindrop impact area with an array of metal nail tips that are uniformly attached to an underwater PVC plate and protrude 1 cm above the water surface.

It is conjectured that the height of the layer with dense clouds of water droplets would be much greater in the field because of the presence of waves and wind. In addition, the liquid water content in the air–sea boundary layer would be even higher than in the laboratory due to bubble and foam bursting and droplets torn off by the wind.

Fig. 6(a) shows a frame of the radar VV signal measured from the rain field while Fig. 6(b) shows the radar VV signal measured from the same raindrop impact area with an array of metal nail tips that are uniformly attached to an underwater polyvinyl chloride (PVC) plate and protrude vertically 1 cm above the water surface. In the latter case, the nail tips are used to mimic the rain-generated stalks on the water surface in the absence of the raindrops and rain-generated secondary droplets. In Fig. 6(a), the raindrop impact area ranges from

0.15 to 0.95 m. As can be seen from Fig. 6, the radar signal in the rain field [Fig. 6(a)] decays with increasing distance from the radar, while the radar signal from the array of the nail tips [Fig. 6(b)] has little variation with the distance for $x < 0.8$ m. The trend difference between these two signals in Fig. 6(a) and (b) is mainly due to the presence of the raindrops and the dense clouds of water droplets generated by the rain. However, since the attenuation due to the rain itself ($\alpha_1$) is much less than that measured from the field ($\alpha_2$), it is suggested that the attenuation due to secondary drops are dominant. In addition, the radar signals obtained from the simulated rain falling on the nail tips (not shown herein) are similar to that shown in Fig. 6(a), showing that the radar signal from the nail tips is significantly attenuated with the distance by the rain. A least squares fit of $|V| = |V|_0 e^{-2\alpha_2' x}$ to the envelope of the radar signal in Fig. 6(a) yields $\alpha_2' = 0.015$ cm$^{-1}$, which is the same order of magnitude as $\alpha_2 = 0.041$ cm$^{-1}$ estimated from the field measurement as shown in the previous section. The difference between $\alpha_2'$ and $\alpha_2$ is mainly due to the following three reasons. First, the radar used in our laboratory is X-band waves while the ASAR images were measured with C-band radar waves. Second, freshwater is used in the laboratory while real oceans have seawater. Third, both the rain and wind conditions in these two cases are different.

From the perspective of the electromagnetic (EM) wave propagation, the attenuation constant $\alpha$ for high-frequency EM waves (C-band 5.3 GHz) in a media with $\sigma \ll \omega\varepsilon$ may be approximated as

$$\alpha \approx \frac{\sigma}{2}\sqrt{\frac{\mu}{\varepsilon}} \tag{19}$$

where $\sigma$ is the electrical conductivity of the media, $\omega$ is the angular frequency of the radar waves, $\mu$ is the permeability, and $\varepsilon$ is the complex dielectric constant.

As $\mu$ is almost the same for all media, the attenuation constant ratio between seawater and air is given as

$$\frac{\alpha_s}{\alpha_a} = \frac{\sigma_s}{\sigma_a}\sqrt{\frac{\varepsilon_a}{\varepsilon_s}} = 1.5 \times 10^{14} \tag{20}$$

where $\varepsilon_a = 1$, and $\sigma_a = 3 \times 10^{-15} \sim 8 \times 10^{-15}$ S/m for the air (we take $\sigma_a = 5 \times 10^{-15}$ S/m). For seawater (temperature of 20°C and salinity of 35 psu), $\varepsilon_s = 43.18$, and $\sigma_s = 4.8$ S/m. Equation (20) shows that the attenuation constant in seawater is about $1.5 \times 10^{14}$ times larger than that in the atmosphere. The medium in the layer near the ocean surface in rain fields is not seawater, but a mixture of air and seawater. Compared with air, the dense seawater droplet cloud is a high conductivity medium and a strong absorber of the radar waves. Thus in this layer, the attenuation would be much greater than that in the atmosphere.

In sum, the air–sea boundary layer generated by rainfall on the ocean surface comprises a region of high attenuation for the radar waves, which is distinct from the case of the air with freshwater raindrops. A laboratory experimental investigation on this air–sea boundary layer in rain fields is underway.

## IV. CONCLUSION

In this paper, a stalk-dominated radar backscattering model for quantifying the dependence of the ocean surface radar return intensity on the rain rate was developed. The model shows that the radar backscattering intensity from the ocean surface is a nonmonotonic function of the average distance between raindrops in the rain field, the radar wave frequency, and the incident angle of radar waves. For light/moderate rain (at low rain rates), the radar backscattering intensity increases with increasing rain rate. For heavy rain (at high rain rates), the radar backscattering intensity decreases with increasing rain rate. The maximum radar backscattering intensity occurs at a rain rate that depends on the radar wave frequency and the incident angle of radar waves.

The model is used to interpret the C-band ASAR images of a rain cell in the Northwest Pacific near the Luzon Strait. The rain cell was also simultaneously observed by the ground-based weather radar. The correlation of the radar backscattering coefficient from the ASAR image with the rain rate that is converted from the reflectivity factor from the ground-based weather radar shows that the radar backscattering coefficient from satellite increases as the rain rate increases, until 24 mm/h. When the rain rate is greater than 24 mm/h, the radar backscattering coefficient measured from satellite decreases as the rain rate increases. The relationship of the radar backscattering with the rain rate is in agreement with the model's calculation.

The air–sea interface in rain fields and its effects on the attenuation of radar backscattering are experimentally studied in the laboratory. It is found that rain generates a layer of dense clouds of seawater droplets close to the ocean surface and the radar backscattering from the stalks is highly attenuated by this layer. Laboratory and field measurements of the damping coefficient $\beta$ under various rain and wind conditions are expected in the future.

The model proposed in this paper is verified by the ASAR and ground-based meteorological data obtained under low wind conditions. However, it should be emphasized that the effects of wind waves, rain-induced ring waves, and raindrops in the atmosphere might dominate the radar backscattering signatures of a rainfall event over the ocean for light rain and/or high winds. In addition, the damping of surface waves by rain-induced turbulence and the attenuation of microwaves by rain in the atmosphere should be taken into account as well. A comprehensive model investigating all these effects is underway.

## APPENDIX
### EXPERIMENTAL SETUP OF RADAR MEASUREMENT IN RAIN FIELD

The experiment was performed in a rain facility that includes an overflow water tank and a rain generator (see Fig. 7(a) and [29]). The overflow water tank is 1.2-m-by-1.2-m square in plan view with a depth of 0.31 m. The tank is constructed of transparent acrylic and the two opposing sidewalls of the tank are 1.27 cm lower than the other two sidewalls. The tank is supported by a short frame that is adjusted so that the upper edges of the two lower sidewalls form a horizontal plane. During the experiment, the tank is operated with a constant water level by maintaining an
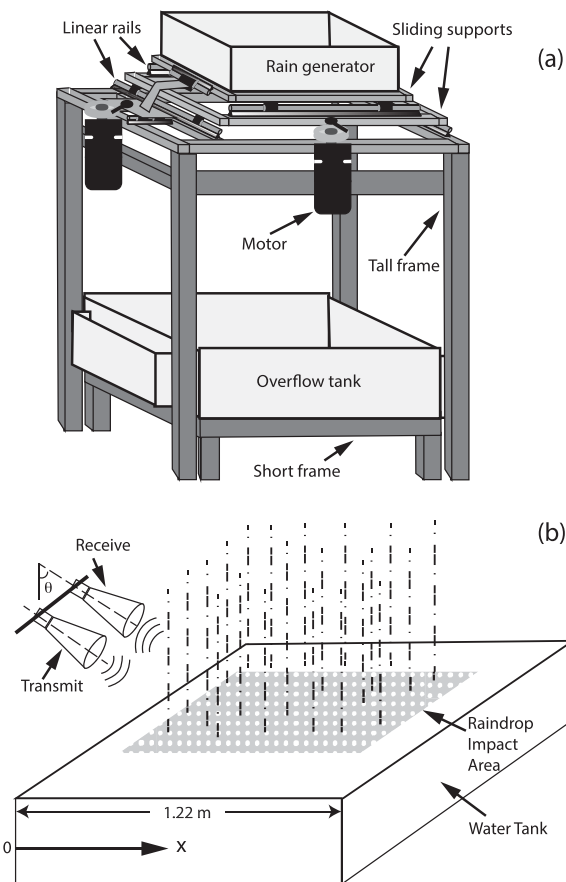
Fig. 7. Schematic showing (a) rain simulation facility from [29] and (b) radar measurement. The drawing is not to scale. The raindrop impact area is 0.8 m long and 0.6 m wide, and $\theta = 55.7°$.

overflow condition at the two lower sidewalls with inflow due entirely to the incoming raindrops.

The rain generator consists of an array of sites for 738 hypodermic needles mounted at the bottom of a rectangular water tank (horizontal dimensions 0.9 m × 0.6 m) that is in turn mounted on a linear traverser system with two horizontal degrees of freedom. The distance between the needles is about 2.54 cm. The needles are 22-gauge, with an inner diameter of 0.41 mm and a length of 6.35 mm. The water in the rain generator was kept at a depth of about 23 cm using an overflow pipe and this produced a rain rate of $R = 340$ mm/h. Each axis of the traverser system consists of two parallel rails, bearings, a servomotor, a crank-piston drive mechanism, and a linear position feedback sensor. The traverser system is mounted on a tall frame and the rain generator is attached to the top motion axis mechanism. The tall frame is attached to the lab ceiling and the side walls to stabilize the entire rain simulation system. The motion of the rain generator is controlled by a computer using the position feedback sensor on each motion axis. In the present study, the rain generator motion was circular with a diameter of 2.54 cm and a frequency of 0.1 Hz. The rain generator was positioned 2.3 m above the free surface of the overflow water tank and the droplet impact speed of the raindrops on the water surface was 5.6 m/s, which is about 72% of the terminal velocity of same-sized raindrops in natural conditions.

An ultrawideband radar similar to that described in [38] and [39] is used in the present study. The radar is based on a fast oscilloscope (Tektronix Model DPO72004B) that samples the radar backscatter in real time at rates of up to 50 GS/s. The short ultrawideband pulse is generated through the use of an ultrafast pulse generator (PSPL Model 4015) and a 6–12 GHz solid-state microwave amplifier. The combination of the amplifier response and the time-domain reflectometer pulse rise time produces microwave pulses with a 3 dB pulsewidth of approximately 0.5 ns, providing a range resolution of approximately 4 cm. In the present study, the system was operated in a dual-polarized mode in which both the copolarized and cross-polarized vertical and horizontal echoes were collected at a per-polarization pulse repetition frequency of 500 Hz. One complete scan of the 1.2 m range swath of the radar was completed at every pulse, with (HH, HV) and (VV, VH) echoes collected on alternate scans. The distance to the center of the rain field on the water surface from the two system antennas (one for transmitting, one for receiving) was 1.6 m, producing a bistatic angle of 9°. The radar was mounted such that it looked down on the water surface in the rain field at an angle of 55.7° relative to the vertical [see Fig. 7(b)].

REFERENCES

[1] L. L. Fu, and B. Holt, "Seasat views oceans and sea ice with synthetic-aperture radar," Nat. Aeronautics Space Admin. (NASA), Jet Propuls. Lab. (JPL), Pasadena, CA, USA, Tech. Rep. 81–120, 1982, p. 179.
[2] A. R. Jameson et al., "SIR-C/X-SAR observations of rain storms," Remote Sens. Environ., vol. 59, no. 2, pp. 267–279, Feb. 1997.
[3] J. Simpson, C. Kummerow, W.-K. Tao, and R. F. Adler, "On the tropical rainfall measuring mission (TRMM)," Meterol. Atmos. Phys., vol. 60, no. 1, pp. 19–36, Mar. 1996.
[4] W. Alpers and C. Melsheimer, "Chapter 17. Rainfall," in Synthetic Aperture Radar Marine User's Manual, C. R. Jackson and J. R. Apel, Eds. Washington, DC, USA: U.S. Department of Commerce, 2004, pp. 355–371.
[5] C. Melsheimer, W. Alpers, and M. Gade, "Simultaneous observations of rain cells over the ocean by the synthetic aperture radar aboard the ERS satellites and by surface-based weather radars," J. Geophys. Res., vol. 106, no. C3, pp. 4665–4677, Mar. 2001.
[6] W. Alpers, C. M. Cheng, Y. Shao, and L. Yang, "Study of rain events over the South China sea by synergistic use of multi-sensor satellite and ground-based meteorological data," Photogrammetric Eng. Remote Sens., vol. 73, no. 3, pp. 267–278, Mar. 2007.
[7] D. Atlas, "Origin of storm footprints on the sea screen by synthetic aperture radar," Science, vol. 266, no. 5189, p. 1364, Nov. 1994.
[8] D. Atlas, "Footprints of storms on the sea: A view from space-borne synthetic aperture radar," J. Geophys. Res., vol. 99, no. C4, pp. 7961–7969, Apr. 1994.
[9] C. Melsheimer, W. Alpers, and M. Gade, "Investigation of mul-tifrequency/multipolarization radar signatures of rain cells over the ocean using SIR-C/X-SAR data," J. Geophys. Res., vol. 103, no. C9, pp. 18867–18884, Aug. 1998, doi: 10.1029/98JC00779.1998.
[10] T. Oguchi, "Electromagnetic wave propagation and scattering in rain and other hydrometeors," Proc. IEEE, vol. 71, no. 9, pp. 1029–1078, Sep. 1983.
[11] F. T. Ulaby, R. K. Moore, and A. K. Fung, Microwave Remote Sensing: Active and Passive, Volume II: Radar Remote Sensing and Surface Scattering and Emission Theory. Reading, MA, USA: Addison-Wesley, 1982.

[12] C. Nie and D. G. Long, "A C-band wind/rain backscatter model," *IEEE Trans. Geosci. Remote Sens.*, vol. 45, no. 3, pp. 621–631, Mar. 2007, doi: 10.1109/TGRS.2006.888457.

[13] F. Xu, X. Li, P. Wang, J. Yang, W. G. Pichel, and Y. Q. Jin, "A backscattering model of rainfall over rough sea surface for synthetic aperture radar," *IEEE Trans. Geosci. Remote Sens.*, vol. 53, no. 6, pp. 3042–3054, Jun. 2015.

[14] R. K. Moore, Y. S. Yu, A. K. Fung, D. Kaneko, G. J. Dome, and R. E. Werp, "Preliminary study of rain effects on radar scattering from water surfaces," *IEEE J. Ocean. Eng.*, vol. 4, no. 1, pp. 31–32, Jan. 1979.

[15] J. P. Hansen, "Rain backscatter tests dispel old theories," *Microw. RF*, vol. 25, pp. 97–102, Jun. 1986.

[16] P. W. Sobieski, C. Craeye, and L. F. Bliven, "Scatterometric signatures of multivariate drop impacts on fresh and salt water surfaces," *Int. J. Remote Sens.*, vol. 20, no. 11, pp. 2149–2166, 1999.

[17] N. Braun, M. Gade, and P. A. Lange, "The effect of artificial rain on wave spectra and multi-polarisation X band radar backscatter," *Int. J. Remote Sens.*, vol. 23, no. 20, pp. 4305–4323, 2002.

[18] M. N. Tsimplis and S. A. Thorpe, "Wave damping by rain," *Nature*, vol. 342, pp. 893–895, Dec. 1989.

[19] M. N. Tsimplis, "The effect of rain in calming the sea," *J. Phys. Oceanogr.*, vol. 22, no. 4, pp. 404–412, 1992.

[20] Y. K. Poon, S. Tang, and J. Wu, "Interactions between rain and wind waves," *J. Phys. Oceanogr.*, vol. 22, pp. 977–987, 1992.

[21] Z. Yang, S. Tang, and J. Wu, "An experimental study of rain effects on fine structures of wind waves," *J. Phys. Oceanogr.*, vol. 27, no. 3, pp. 419–430, 1997.

[22] L. Bliven, H. Branget, P. W. Sobieski, and J. P. Giovanangeli, "An analysis of scatterometer returns from a water surface agitated by artificial rain: Evidence that ring-waves are the main feature," *Int. J. Remote Sens.*, vol. 14, no. 12, pp. 2315–2329, 1993.

[23] L. F. Bliven, P. W. Sobieski, and C. Craeye, "Rain generated ring-waves: Measurements and modeling for remote sensing," *Int. J. Remote Sens.*, vol. 18, no. 1, pp. 221–228, 1997.

[24] D. Lemaire, L. F. Bliven, C. Craeye, and P. Sobieski, "Drop size effects on rain-generated ring-waves with a view to remote sensing applications," *Int. J. Remote Sens.*, vol. 23, no. 12, pp. 2345–2357, 2002.

[25] B. Le Méhauté, and T. Khangaonkar, "Dynamic interaction of intense rain with water waves," *J. Phys. Oceanogr.*, vol. 20, no. 12, pp. 1805–1812, 1992.

[26] G. Zhang, X. Li, W. Perrie, B. Zhang, and L. Wang, "Rain effects on the hurricane observations over the ocean by C-band synthetic aperture radar," *J. Geophys. Res., Oceans*, vol. 121, no. 1, pp. 14–26, Jun. 2016. doi: 10.1002/2015JC011044.

[27] R. F. Contreras and W. J. Plant, "Surface effect of rain on microwave backscatter from the ocean: Measurements and modeling," *J. Geophys. Res.*, vol. 111, C08019, Aug. 2006, doi: 10.1029/2005JC003356.

[28] L. B. Wetzel, "On the theory of electromagnetic scattering from a raindrop splash," *Radio Sci.*, vol. 25, no. 6, pp. 1183–1197, Nov./Dec. 1990.

[29] X. Liu, Q. Zheng, R. Liu, D. Wang, J. H. Duncan, and S.-J. Huang, "A study of radar backscattering from water surface in response to rainfall," *J. Geophys. Res.*, vol. 121, no. 3, pp. 1546–1562, Mar. 2016, doi: 10.1002/2015JC010975.

[30] J. S. Erkelens, V. K. C. venema, H. W. J. Russchenberg, and L. P. Ligthart, "Coherent scattering of microwaves by particles: Evidence from clouds and smoke," *J. Atmos. Sci.*, vol. 58, no. 9, pp. 1091–1102, 2001.

[31] C. A. Knight and L. J. Miller, "Early radar echoes from small, warm cumulus: Bragg and hydrometeor scattering," *J. Atmospheric Sci.*, vol. 55, no. 18, pp. 2974–2992, 1998.

[32] R. R. Rogers and W. O. J. Brown, "Radar observations of a major industrial fire," *Bull. Amer. Meteor. Soc.*, vol. 78, no. 5, pp. 803–814, 1997.

[33] A. R. Jameson and A. B. Kostinski, "Partially coherent backscatter in radar observations of precipitation," *J. Atmos. Sci.*, vol. 67, no. 6, pp. 1928–1946, 2010.

[34] A. R. Jameson and A. B. Kostinski, "Direct observations of coherent backscatter of radar waves in precipitation," *J. Atmos. Sci.*, vol. 67, pp. 3000–3005, Jun. 2010.

[35] A. R. Jameson, "Statistical reliability of neighboring range bin estimates of coherent fractional contributions to radar backscattered power," *J. Appl. Meteor. Climatol.*, vol. 50, no. 3, pp. 745–749, 2011.

[36] A. R. Jameson, "Precipitation Bragg Scatter in Radar Observations at Nadir," *J. Appl. Meteor. Climatol.*, vol. 50, pp. 1981–1984, Sep. 2011.

[37] L. J. Battan, *Radar Observation of the Atmosphere*. Chicago, IL, USA: Univ. Chicago Press, 1973.

[38] M. A. Sletten and D. B. Trizna, "An ultrawideband, polarimetric radar for the study of sea scatter," *IEEE Trans. Antennas Propag.*, vol. 42, no. 11, pp. 1461–1466, Nov. 1994.

[39] M. A. Sletten, J. C. West, X. Liu, and J. H. Duncan, "Radar investigations of breaking water waves at low grazing angles with simultaneous high-speed optical imagery," *Radio Sci.*, vol. 38, no. 6, 1110, Dec. 2003, doi: 10.1029/2002RS002716.

**Xinan Liu** (M'16) received the B.S. degree in mathematics from Jilin University, Changchun, China, in 1986, the M.S. degree in physical oceanography from the Ocean University of China, Qingdao, China, in 1989, and the Ph.D. degree in mechanical engineering from the University of Maryland at College Park, College Park, MD, USA, in 2002.

From 1989 to 1997, he was a Research Scientist with the First Institute of Oceanography, State Oceanic Administration, Qingdao, where he was involved in the field measurements of coastal dynamics on sand ocean beach, interaction between sea waves and vertical breakwaters, and shoaling of nonlinear random waves. Since 2002, he has been with the University of Maryland at College Park, where he is currently a Research Associate Professor with the Department of Mechanical Engineering and teaches undergraduate courses in electronics and instrumentation, and fluid mechanics. He has been involved in using radar for understanding the fundamental physics of a number of flow phenomena on the ocean surface. His current research interests include radar backscattering of rough water surface, the response of the ocean surface to rainfall, water wave breaking, surfactant dynamics, and low-frequency waves in coastal areas.



**Quanan Zheng** received the B.S. degree in physics from Jilin University, Changchun, China, and the Ph.D. degree in physical oceanography from the Institute of Oceanography, Chinese Academy of Sciences, Qingdao, China.

He was with the First Institute of Oceanography, State Oceanic Administration, Qingdao, and the University of Delaware, Newark, DE, USA. Since 2004, he has been with the University of Maryland at College Park, College Park, MD, USA, where he is currently a Senior Research Scientist with the Department of Atmospheric and Oceanic Sciences. He has over 125 publications. His current research interests include ocean remote sensing (physics, data interpretation, applications, and laboratory simulation), ocean surface processes (wind friction, wave spectra, skin layer physics, and surfactant effects), upper ocean dynamics (internal wave dynamics and ocean-atmospheric coupling), mesoscale ocean dynamics, solitary waves in the atmosphere and ocean, and space shuttle photographic applications.



**Ren Liu** (S'16) received the B.S. degree in mechanical engineering and mathematics from the University of Maryland at College Park (UMCP), College Park, MD, USA, in 2008, where he is currently pursuing the Ph.D. degree in mechanical engineering.

He joined the Hydrodynamic Laboratory, UMCP, in 2009. His current research interests include the surface features induced by the impact of raindrops on the ocean and their effects on the backscattering of satellite radar.

**Mark A. Sletten** (SM'04) received the B.S., M.S., and Ph.D. degrees in electrical engineering from the University of Wisconsin–Madison, Madison, WI, USA, in 1984, 1987, and 1991, respectively.

He was involved in a real-aperture radar study of the Chesapeake Bay outflow plume, and the development of a lightweight, multiband, and interferometric SAR for use on a light aircraft. Since 1991, he has been with the Naval Research Laboratory (NRL), Washington, DC, USA, where he is involved in radar-based remote sensing research. He has also conducted numerous field experiments that investigate the use of interferometric SAR systems for measuring ocean surface currents and mapping the space-time evolution of submesoscale oceanic eddies. His present emphasis is on the development of multiphase-center SAR systems and algorithms for the measurement of scene motion. Beginning in FY17, he will lead an NRL program designed to develop maritime applications for UHF SAR.

Dr. Sletten was a recipient of the Delores M. Etter Top Navy Scientists and Engineers of the Year Award.

**James H. Duncan** received the B.S. degree in mechanical engineering from Brown University, Providence, RI, USA, in 1971, and the Ph.D. degree in 1979, geophysical fluid dynamics from The Johns Hopkins University, Baltimore, MD, USA, in 1979.

He was a Research Scientist with Hydronautics, Inc., and Flow Research Company, Laurel, MD, USA. In 1987, he joined as a Faculty Member with the Department of Mechanical Engineering, University of Maryland at College Park, College Park, MD, USA, where he is currently a Professor of Mechanical Engineering. His research has included the studies of fundamental aspects of breaking waves, cavitation bubbles, fluid-structure interactions, and computer vision.

Dr. Duncan is a Fellow of the American Physical Society (APS) and has served in a number of roles on the Executive Committee of the Division of Fluid Dynamics of APS, including the Division Chairman in 2015. He was a recipient of a number of teaching and research awards at the University of Maryland including the Poole and Kent Senior Faculty Teaching Award, the Distinguished Scholar Teacher Award, and the Wilson H. Elkins Professorship. Since 2010, he has been serving as an Associate Editor of the *Journal of Fluid Mechanics*.